# Radiation-Induced Charge Collection Comparison Between Silicon and Silicon Carbide Avalanche Photodiodes

Nathaniel J. Karom, *Graduate Student Member, IEEE,* Dennis R. Ball, *Senior Member, IEEE,* Eden Teo, *Student Member, IEEE,* Anurag R. Veluri, *Graduate Student Member,* Akin Akturk, Zeynep Dilli, *Member, IEEE,* Neil Goldsman, Bryce Galey, Usama Khalid, Mitchell Gross, Ryan Purcell, *IEEE,* Richard H. Nederlander, *Member, IEEE,* Phoenix M. Harris, Michael W. McCurdy, *Senior Member, IEEE,* Ronald D. Schrimpf, *Life Fellow, IEEE,* Daniel M. Fleetwood, *Life Fellow, IEEE,* James M. Trippe, *Senior Member, IEEE,* Robert A. Reed, *Fellow, IEEE* and Sharon M. Weiss, *Senior Member, IEEE*

***Abstract*—Avalanche photodiodes (APDs) are essential to multi-messenger astronomy (MMA) space-based observatories for detecting low-intensity signals across the electromagnetic spectrum, often paired with scintillators for particle detection. However, the harsh radiation environment of space threatens to mask or imitate legitimate signals via single-event transients (SETs). This work investigates charge collection from 3.4 MeV alpha-induced SETs in Si and 4H-SiC APDs, which exhibit vastly different behavior. Relative to 0 V, the Si-APD shows suppressed gain (1.5×) while the SiC-APD shows significant gain (17×) near electrical breakdown. Calibrated Sentaurus TCAD simulations of both alpha strikes and optical generation reveal that both devices develop substantial space charge perturbations along the ion track, but only the Si-APD shows a corresponding collapse of the electric field and suppression of impact ionization in the avalanche region. We attribute this difference to device geometry. In the Si-APD, the ion track overlaps the high-field avalanche region, driving the local field collapse. In the SiC-APD, the higher epitaxial region doping confines the avalanche region to a micrometer-thin layer, leaving the high field relatively undisturbed. Holes then reach the avalanche region as a low-density, distributed flux that resembles optically-generated carriers. These results clarify differences in the radiation response of Si and SiC-APDs for future space-based observatory applications.**

***Index Terms*—Avalanche photodiodes (APDs), 4H-Silicon Carbide (4H-SiC), single-event transients (SETs), impact ionization, charge collection, radiation effects, silicon photonics, multi-messenger astronomy (MMA)**

## I. Introduction

The advent of multi-messenger astronomy (MMA) has expanded our ability to study the most energetic transient events in the universe. Famous examples of MMA in action are the coincident detection of gravitational waves and short gamma-ray bursts from the neutron star merger GW170817 [1] and high-energy neutrinos coupled with UV/optical/X-ray observations of the tidal disruption event AT2019fdr [2]. More recently, the Habitable Worlds Observatory (HWO) under development at NASA plans to use MMA to investigate the atmospheric makeup of exoplanets and detect organic molecules [3], [4]. Space-based observatories capable of detecting signals across the electromagnetic spectrum are therefore essential infrastructure for MMA. These instruments demand photodetectors with high sensitivity, low noise, and internal gain to resolve faint signals. Avalanche photodiodes (APDs) fulfill this requirement through avalanche multiplication, enabling low-light sensitivity across a wide spectral range.

Silicon APDs (Si-APDs) play a mature role in both particle and light detection. Coupled to a scintillating material emitting in the visible spectrum, Si-APDs can detect a variety of particles such as neutrons, protons, and even gamma-ray and X-ray photons [5], [6], [7]. This coupling is invaluable because it allows a single detector architecture to detect multiple species of radiation by varying the scintillating material. By manipulating the doping profile and therefore the electric field

This work was supported by the National Science Foundation (NSF) Industry-University Cooperative Research Center (IUCRC) Electronic-Photonic Integrated Circuits for Aerospace (EPICA) award #2052742, the Establishing Multimessenger astronomy Interdisciplinary Training (EMIT) award #2125764, and the NSF EPICA industry advisory board (IAB).

Nathaniel J. Karom, Ronald D. Schrimpf, Daniel M. Fleetwood, Robert A. Reed, and Sharon M. Weiss are with the Department of Physics and Astronomy, Vanderbilt University, Nashville, TN 37235 USA (email: nathaniel.j.karom@vanderbilt.edu; ron.schrimpf@vanderbilt.edu; dan.fleetwood@vanderbilt.edu; robert.reed@vanderbilt.edu; sharon.weiss@vanderbilt.edu).

Dennis R. Ball, Eden Teo, Anurag R. Veluri P., Phoenix M. Harris, Mike McCurdy, Ronald D. Schrimpf, Daniel M. Fleetwood, James M. Trippe, Robert A. Reed, and Sharon M. Weiss are with the Department of Electrical and Computer Engineering, Vanderbilt University, Nashville, TN 37235 USA (email: scooter.ball@vanderbilt.edu; eden.teo@vanderbilt.edu; anurag.reddy.veluri@vanderbilt.edu; phoenix.harris@vanderbilt.edu; mike.mccurdy@vanderbilt.edu; james.m.trippe@vanderbilt.edu).

Akin Akturk, Zeynep Dilli, Neil Goldsman, Bryce Galey, Usama Khalid, Mitchell Gross, and Ryan Purcell are with CoolCAD Electronics, Greenbelt, MD 20770 USA (email: akin.akturk@coolcadelectronics.com; zeynep.dilli@coolcadelectronics.com; neil.goldsman@coolcadelectronics.com; bryce.galey@coolcadelectronics.com; usama.khalid@coolcadelectronics.com; mitchell.gross@coolcadelectronics.com; ryan.purcell@coolcadelectronics.com).

Richard H. Nederlander is with NASA, Kennedy Space Center (email: richard.h.nederlander@nasa.gov).

profile, specific wavelengths of light in the near-UV and visible spectrum can be amplified and detected [8], [9]. Thus, Si-APDs are commonly used in high-energy environments such as on CubeSats equipped with a scintillator to measure the radiation flux of different regions in space [7], [10].

While Si-APDs are useful for detecting visible light, capturing the full UV spectrum requires a detector optimized for UV. Wide-bandgap semiconductors such as 4H silicon carbide (4H-SiC) offer characteristics well-suited for this role. With a bandgap of ~3.25 eV, approximately three times that of silicon, SiC-APDs exhibit peak photoresponsivity in the UV and near-zero response in the visible spectrum [9]. This "solar blindness" coupled with high avalanche gain and low dark current is essential for detecting faint UV transients in space. Like Si-APDs, these devices can also benefit from scintillators, as UV-emitting scintillators coupled to SiC-APDs allow particle detection [11]. Together, scintillator-coupled Si-APDs and SiC-APDs can broadly span the electromagnetic range demanded by multi-messenger observations.

The space radiation environment poses a significant challenge for both detector types. Energetic heavy ions traversing an APD deposit charge along their track via direct ionization, generating electron-hole pairs (EHPs) that drift under electric field and are collected at device terminals. If this charge is deposited or drifts into the high-field avalanche region, it can be further amplified through impact ionization. The severity of these single-event transients (SETs) depends on a variety of factors, including the ion linear energy transfer (LET), the ion's angle of incidence relative to the avalanche region, device bias, and structure of the avalanche region [12], [13].

SETs are problematic for MMA applications in two ways. First, a radiation-induced signal could be indistinguishable from a legitimate astrophysical event, producing a false positive. Second, a valid signal arriving during the charge collection window of a SET may be masked or distorted, producing a false negative [14], [15]. Ironically, the same avalanche multiplication mechanism that gives APDs their low-light sensitivity advantage can also amplify radiation-induced charge, potentially leading to runaway multiplication and device burnout. The severity and character of this response is strongly dependent on device material and structure, motivating a comparative investigation of how different APD technologies respond to the same radiation environment [16].

Despite the maturity of Si-APDs in space applications [17], [18], the mechanisms governing SET response, including the dependence of collected charge and gain on applied bias and ion LET, are not fully understood. Laird *et al.* investigated heavy ion charge collection mechanisms in $N^+$-P Si-APDs and discussed the quenching of impact ionization due to space-charge screening [19]. The quenching is attributed to the high minority carrier diffusivity in the drift region, allowing the injected charge to be promptly collected before significant impact ionization occurs in the perturbed electric field at the end of the ion track. However, they suggest that $P^+$-N Si-APDs may suffer enhanced gain as the minority carrier in the drift region would be holes, which have ~1/3 the mobility of electrons in Si. The slower-moving holes would spend more time within the perturbed field region, giving impact ionization a longer window to act before the charge is collected. Whether this produces increased gain also depends on the ionization coefficients since holes ionize less readily than electrons in Si.

Although heavy ion irradiation has been performed on SiC power devices [20], [21], SiC-APDs lack experimental testing. Given their thinner structure, higher peak electric field, and higher EHP generation energy (7.78 eV vs. 3.69 eV in Si), it is likely that these devices will respond differently to a SET than their Si counterparts. Makino *et al.* investigated alpha-induced charge collection mechanisms in 4H-SiC Schottky barrier diodes (SBDs) and reported charge enhancement in devices with 30 μm epitaxial region thickness [22]. They attribute this to local field enhancement along the ion track sufficient to drive additional impact ionization and/or trap-assisted tunneling. However, the absence of an avalanche region in SBDs makes the transferability of this mechanism to APDs uncertain. Zhen *et al.* investigated single-event burnout simulations in 4H-SiC APDs with a 0.9 μm epitaxial region thickness and analyzed radiation hardening mechanisms [16]. A direct experimental SET comparison between Si and SiC-APDs under identical irradiation conditions is essential to inform the design of radiation-tolerant multi-messenger observatories.

In this work, we compare the differences in charge collection between Si- and SiC-APDs during 3.4 MeV alpha particle irradiation. We find that the devices behave differently under alpha irradiation, with Si-APDs showing minimal gain (~1.5×) and SiC-APDs showing significant gain (~17×) when close to electrical breakdown. Calibrated TCAD simulations were conducted to investigate the physical mechanisms behind the differences in charge collection in the two devices. We attribute the lower gain in the Si-APD to significant space charge

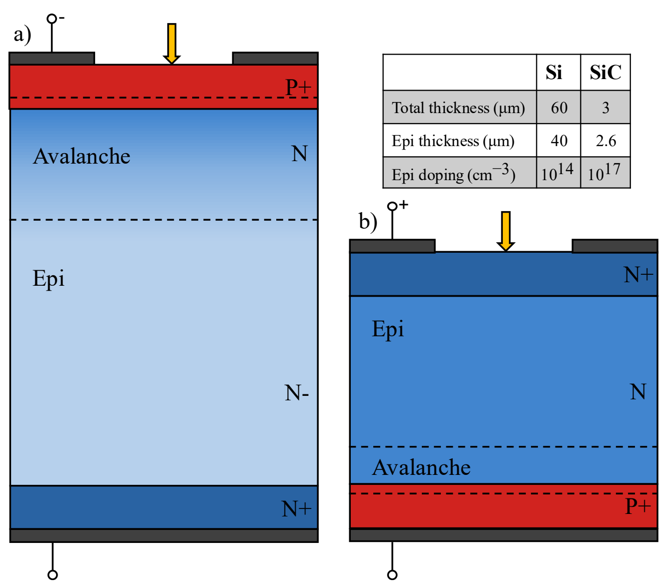


| | Si | SiC |
|---|---|---|
| Total thickness (μm) | 60 | 3 |
| Epi thickness (μm) | 40 | 2.6 |
| Epi doping ($cm^{-3}$) | $10^{14}$ | $10^{17}$ |

Fig. 1. Structure and doping profiles for the a) Si-APDs and b) SiC-APDs used in this study. The impact ionization process for the desired carrier (electrons in Si, holes in SiC) is depicted. The region where significant avalanching occurs is denoted by the dashed lines. The table compares the thickness and approximate doping of the epitaxial region of each device. The images do not reflect the actual scale of the devices.

perturbations, quenching impact ionization and promoting carrier recombination via Shockley-Read-Hall (SRH) and Auger processes. In contrast, the SiC-APD shows minimal space charge perturbations, allowing for increased impact ionization in the high-field ion strike region. These results account for the observed experimental differences in SET responses between Si and SiC-APDs.

## II. Device Structures and Methods

### *A. Devices Under Test (DUTs)*

The Si-APDs investigated in this study are commercial Hamamatsu $P^+$-N Si-APDs (S8664-02K) with a breakdown voltage of 424 V and an effective photosensitive active area of 0.03 $mm^2$ [23]. This active area is where "a typical gain can be obtained," so the actual active region may be larger. The doping profile was obtained via spreading resistance analysis and comparison to the known device structure [5]. Fig. 1(a) shows that the device consists of a thin $P^+$ entrance layer followed by a ~40 μm lightly-doped N-type drift region and an $N^+$ back contact. Under reverse bias, electrons generated in the high-field $P^+$-N junction depletion region undergo impact ionization, producing a cascading multiplication effect that persists until carriers exit the high-field region. Electrons are the preferred carrier for impact ionization in silicon due to the large ionization coefficient ratio $\alpha/\beta \approx 31$ at $E = 2.0 \times 10^5\ V/cm$, where $\alpha$ and $\beta$ are the electron and hole ionization coefficients, respectively [24]. The device exhibits a peak responsivity of ~17 A/W at 580 nm. These devices are supplied with a borosilicate glass window that acts as an anti-reflective layer to maximize photosensitivity. This window was removed by the manufacturer at our request to allow alpha particles to reach the device without stopping in the window.

The SiC-APDs investigated in this study are commercial CoolCAD SiC-APDs (CCSiCUVAPD1p1) with a breakdown voltage of 179 V and an active area of 0.019 $mm^2$ [25]. The doping profile was inferred from similar device structures in the literature and from *I-V* measurements [8]. Fig. 1(b) shows that the device consists of a thin $N^+$ entrance layer, a ~2.6 μm lightly-doped N-type drift region, and a $P^+$ contact layer above an $N^+$ substrate (not pictured). In 4H-SiC, holes are the preferred carrier for impact ionization due to the large ionization coefficient ratio $\beta/\alpha \approx 27$ at $E = 2.5 \times 10^6\ V/cm$ [8], [26]. Under reverse bias, holes generated in the depleted epitaxial region drift into the high-field region and undergo impact ionization. The device exhibits a peak responsivity at 270 nm. Unlike the Si-APDs, these devices are not supplied with an anti-reflective coating.

The Si-APDs were soldered to a custom-made printed circuit board (PCB) equipped with solder-mounted BNC terminals for electrical connections. Due to the absence of solderable leads on the SiC-APD package, each die was mounted using silver paste onto a separate custom-made PCB equipped with solder-mounted SMA terminals, and the anode and cathode bond pads were wire bonded to the PCB using 0.7 mil gold wire bonds. A total of three Si-APDs and two SiC-APDs were prepared in this manner for irradiation testing.

The *I-V* characteristics of each device were measured under both dark and illuminated conditions using a Keysight B1505A power device analyzer. The high-voltage SMU (HVSMU) was used for each device to reach breakdown voltage. Dark current measurements were performed in total darkness and at ambient room temperature (~25 ºC), with measured dark currents on the order of $10^{-7}$ A for the Si-APD and $10^{-10}$ A for the SiC-APD near breakdown. Illuminated measurements were performed using 525 nm and 320 nm LEDs for the Si and SiC-APDs, respectively, selected to coincide within the photosensitivity region of each device. These optical gain measurements serve as a baseline for comparison against the ion-induced charge collection results presented in Section III.

### *B. Experimental Setup*

A pulse height analysis (PHA) experimental setup (shown in Fig. 2) was used to measure the energy spectrum of the charge collected by each APD. Each DUT was placed in a vacuum chamber to prevent alpha particle energy loss in air, with the cathode forward biased using an Ortec 428 detector bias supply and the anode connected to earth ground. The resulting current transient was converted to a voltage pulse by an Ortec 142A charge-sensitive preamplifier, amplified 100× and shaped with a 3 μs shaping time by an Ortec 671 shaping amplifier, and binned into a pulse height spectrum by an Amptek MCA8000D multichannel analyzer (MCA) based on pulse amplitude.

The PHA system was calibrated using an Ortec Si surface barrier detector (model no. U-011-050-300) and a 0.1 μCi unsealed Am-241 button source with a peak alpha energy of 5.5 MeV [13]. Using this calibration, the effective alpha energy

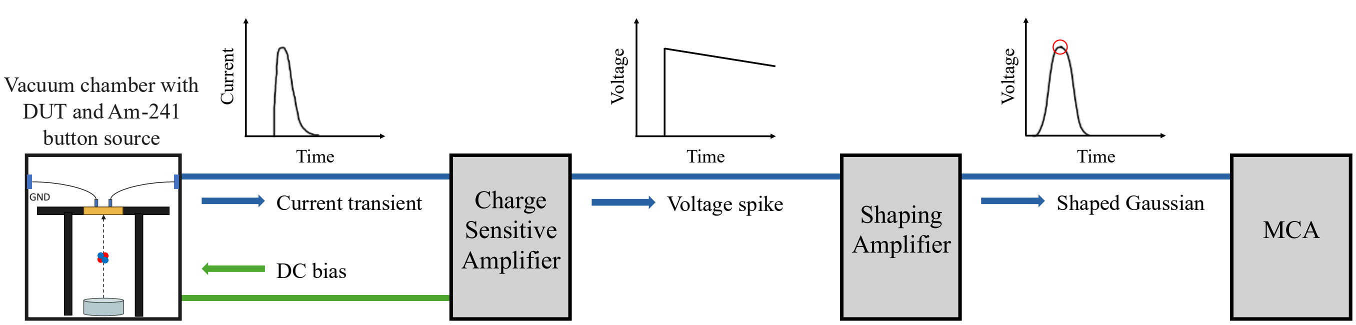


Fig. 2. Schematic diagram of the pulse height analysis experimental setup. The Am-241 button source and APD are contained in a vacuum chamber. The current transient resulting from alpha-induced charge is converted to a voltage shift by the charge sensitive amplifier and shaped into a Gaussian profile by the shaping amplifier. The height of the Gaussian distribution is binned in a histogram via the MCA, allowing for *in-situ* measurements of collected charge.

of a 59.6 μCi sealed Am-241 button source was measured to be ~3.4 MeV, with the energy reduction attributed to energy loss in the sealed source cover. The 59.6 μCi source was used for all device irradiation to maximize particle flux. The source was mounted on a custom stage parallel to the DUT to maximize normal incidence onto the active region, positioned ~1 cm from the DUT. This distance led to a count rate of ~170 counts/second (dead-time $< 0.4\%$) for the Si-APD and ~8 counts/second (dead-time $< 0.3\%$) for the SiC-APD. All measurements were performed in a vacuum chamber in total darkness, at ambient room temperature (25 ºC), and at a pressure of $\sim 10^{-3}$ mbar.

During irradiation, the device bias was incremented in steps of -50 V and -25 V for the Si- and SiC-APDs, respectively, to characterize collected charge as a function of applied bias. Testing was stopped at -400 V for the Si-APD and -175 V for the SiC-APD to avoid reaching the breakdown voltage of each device (-424 V and -179 V, respectively). Each device was irradiated until a minimum of 200 counts were collected in a single bin. Following irradiation, the *I-V* characteristics of each device were remeasured to assess any radiation-induced degradation. Pre- and post-irradiation dark *I-V* measurements showed no significant change in breakdown voltage or dark current for either device.

### *C. TCAD Simulation Framework*

Sentaurus TCAD simulations were employed to investigate the physical mechanisms underlying the differences in charge collection between the two devices [27]. The Si-APD doping profile was directly measured via spreading resistance analysis and used to construct the simulation structure. Since a direct doping profile measurement was not available for the SiC-APD, its structure was instead inferred from similar device structures reported in the literature and refined by tuning the epitaxial region doping concentration to match the experimentally measured breakdown voltage [8]. Both models show close agreement with manufacturer dark current, photosensitivity, and optical gain.

Carrier transport was modeled using doping-dependent mobility, high-field saturation mobility, and carrier-carrier scattering to accurately capture transport behavior across the range of carrier densities encountered during an ion strike. To account for carrier generation and recombination, doping-dependent SRH, Auger, and impact ionization models were implemented [8], [28]. Bandgap narrowing was included to account for the effect of heavy doping on the local band structure in the highly-doped contact regions. A constant background carrier generation rate of $10^{12}$cm$^{-3}$s$^{-1}$ was applied to maintain numerical stability during simulation. All simulations utilized 2-D cylindrical symmetry to reduce computational overhead. The total collected charge ($Q_{total}$) was calculated by integrating the output current over the transient duration, with each simulation run until the current at each contact returned to its pre-strike dark current value to ensure complete charge collection.

For the heavy ion simulations, SRIM was used to determine the LET vs. depth profile of a 3.4 MeV alpha particle in both Si and SiC [29]. Due to the difference in density and stopping power between the two materials, the Bragg peak lies ~13 μm in Si and ~8 μm in SiC. The resulting LET vs. depth profiles were imported into Sentaurus Device with a 0.5 μm step size and 0.05 μm track radius. The ion strike was positioned at the point of cylindrical symmetry, which is equivalent to the ion striking the center of the device at normal incidence. For the optical simulations, a monochromatic source with a wavetime of 1 ps was positioned normal to the top of each device. Wavelengths of 525 nm and 320 nm were chosen to match the wavelengths used in the illuminated *I-V* characterization described in Section 2A.

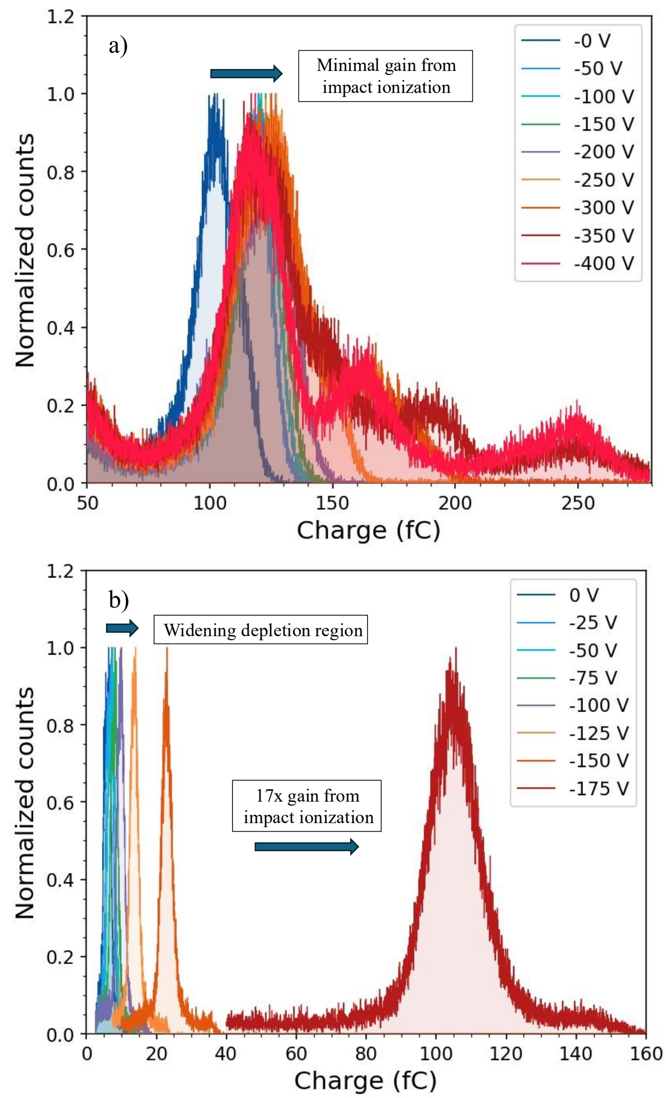


Fig. 3. Output charge collection histogram from the PHA experimental setup described in Section II.B for the a) Si-APD and b) SiC-APD as a function of applied bias. Each count corresponds to charge collected from a SET. The linear increase at lower biases is attributed to increasing depletion region width, which reduces carrier recombination. For the Si-APD, there is little increase in collected charge as a function of bias. In contrast, the SiC-APD shows an exponential increase in charge collection as a function of bias. The physics behind the differences in charge collection are discussed in Section III.B.

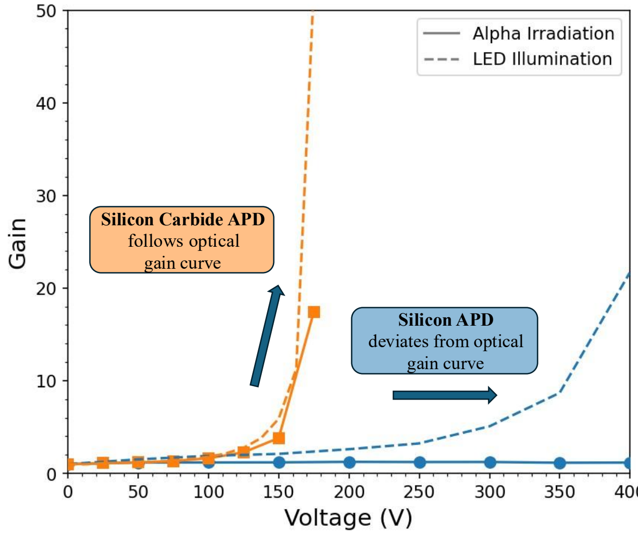


Fig. 4. Alpha-induced (solid line) and optically-induced (dashed line) gain as a function of applied reverse bias for the Si-APD (blue circles) and SiC-APD (orange squares). The Si-APD's gain deviates from the optical gain curve while the SiC-APD's gain closely follows the optical gain curve. This suggests different charge collection mechanisms between the two devices.

## III. Results and Discussion

### A. Experimental Results

Fig. 3 shows the output MCA spectra of alpha-induced collected charge for a) Si-APD and b) SiC-APD, normalized to the peak channel count, at each applied bias. To quantify the change in charge collection as a function of bias, we define gain $G$ as the ratio of collected charge $Q$ at a given reverse bias to the collected charge at 0 V:

$$G = \frac{Q(V)}{Q(0V)}. \tag{1}$$

We note that this definition uses 0 V as the unity-gain reference, which captures both the depletion-width and impact ionization contributions to increased charge collection as bias increases. This allows direct comparison to be made between alpha-induced gain $G_{alpha}$ and optically-induced gain $G_{opt}$. Fig. 4 shows $G$ as a function of applied bias for both devices, where $Q(V)$ is taken as the charge at the peak channel of the MCA spectrum. The photocurrent gain is calculated from the I-V characterization discussed in Section II.A.

At lower biases, both devices show a slight increase in charge collection, which we attribute to the widening depletion region. Carriers generated within the depletion region are swept rapidly to their respective contacts, reducing the probability of recombination. As the depletion region widens with increasing bias, a greater fraction of alpha-induced charge avoids recombination and is collected. The behavior of the two devices diverges significantly beyond −200 V and −100 V for Si- and SiC-APDs, respectively. Despite electric fields sufficient to incite significant impact ionization (supported by $G_{opt} \approx 2$ at −250 V in Fig. 4), the Si-APD shows minimal gain increase with applied bias. In contrast, the SiC-APD exhibits an exponential increase in gain that closely tracks the $G_{opt}$ vs. voltage curve, indicating that alpha-induced free carriers undergo impact ionization in a similar manner to optically generated carriers.

The measured full width at half maximum (FWHM) of the collected charge spectrum, shown in Fig. 3, provides additional insight into the charge collection mechanisms in both devices. Since impact ionization is a stochastic process, an increase in FWHM with applied bias reflects an increasing impact ionization rate, as secondary carriers generated by impact ionization can themselves trigger further multiplication. A clear trend is observed in the SiC-APD as the FWHM broadens significantly as a function of bias (2 fC at 0 V vs. 16 fC at −175 V). The sharp increase in FWHM specifically between −150 V and −175 V reflects the strong, exponential dependence of the ionization coefficients on electric field magnitude near breakdown, where small increments in bias produce large changes in gain.

The Si-APD FWHM broadens slightly at lower biases (20 fC at 0 V vs. 29 fC at −200 V), consistent with a modest increase in impact ionization rate. However, beyond −200 V, the high-charge tail of the spectrum begins to broaden. Beyond −300 V, the spectrum separates into discrete secondary peaks. These secondary peaks were reproducibly observed at the same collected charge values across multiple irradiated Si-APDs. To probe the origin of these features, the angle of the alpha source relative to the Si-APD was varied. At oblique incidence, the secondary peaks shifted towards the primary peak. This angular dependence is consistent with a pathlength-dependent gain mechanism. No secondary peaks are observed in the SiC-APD spectrum, which we attribute to the alpha particle passing completely through the thin epitaxial region. The analysis presented here focuses on the primary peak; full characterization of the secondary peak mechanism is left for future work.

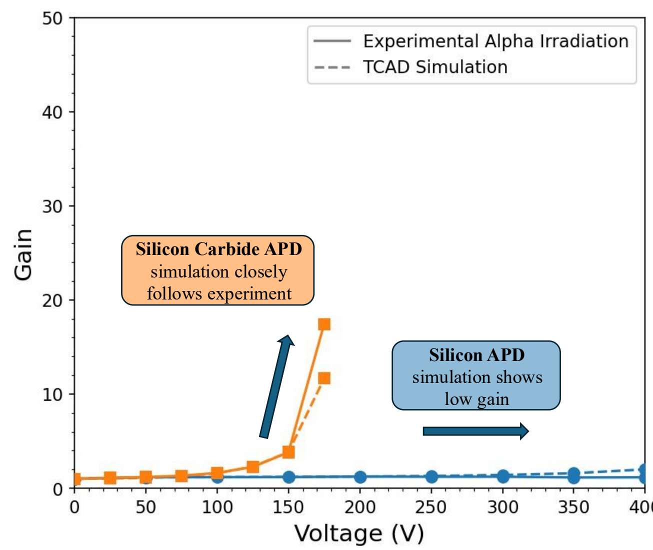


Fig. 5. Experimental (solid line) and simulated (dashed line) alpha-induced gain as a function of applied reverse bias for the Si-APD (blue circles) and SiC-APD (orange squares). Both simulations follow the experimental gain curve at lower biases and slightly deviate at higher biases. We attribute this deviation to sensitive ionization coefficients and missing device information.

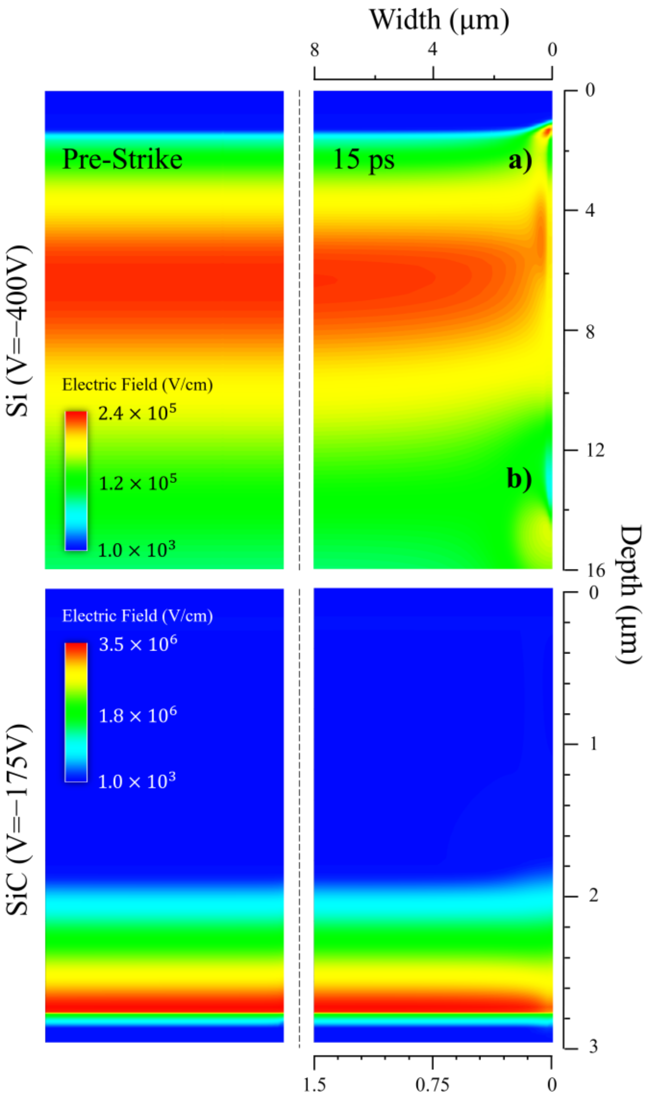


Fig. 6. Electric field distributions near breakdown in Si- (top) and SiC-APDs (bottom) before the ion strike (left) and 15 ps after the ion strike (right). The ion strike occurs at the top right corner of the device, equivalent to the center of the device in cylindrical symmetry. Depth and width of the device cut are labeled on the top and right side. Significant electric field perturbation is observed in the Si-APD, denoted by a) and b). Minimal electric field perturbation is observed in the SiC-APD.

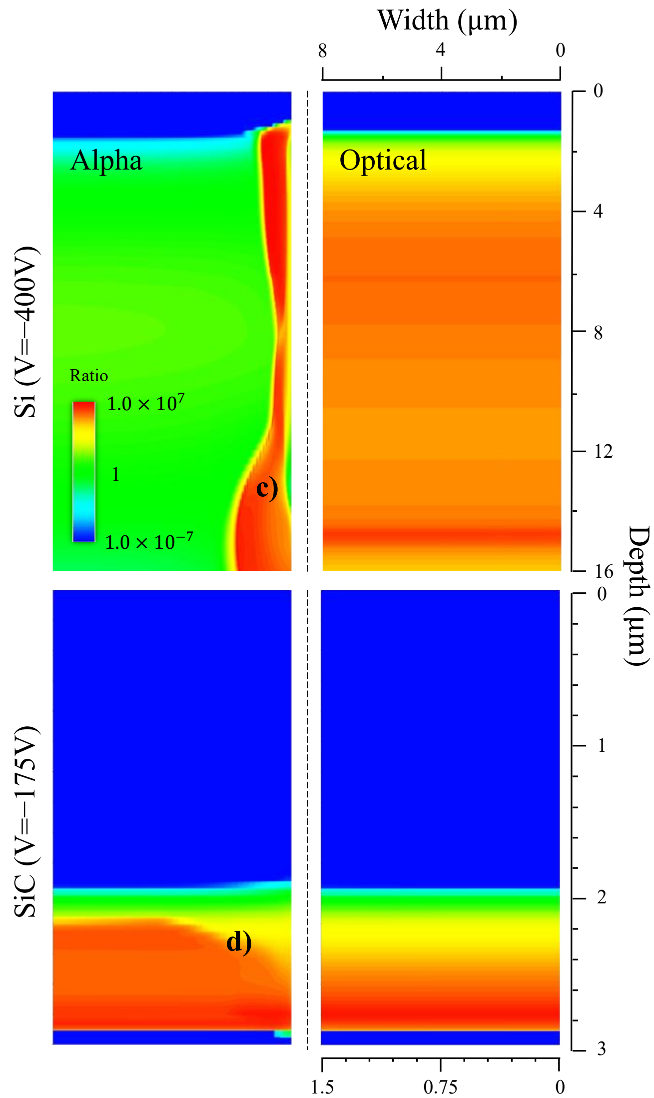


Fig. 7. Ratio of impact ionization rate and net recombination rate in the Si-APD (top) and SiC-APD (bottom) 15 ps after the ion strike (left) and under steady-state optical generation (right). Depth and width of the device cut are labeled on the top and right side. The wavelengths in Section II.A are used. The Si-APD behaves differently under alpha irradiation compared to optical generation, with recombination dominating in the core of the ion track, denoted by c). The SiC-APD behaves similarly in both cases, with holes from the ion strike drifting into the high-field region and undergoing significant impact ionization, denoted by d).

Although these devices are designed to have peak optical gain exceeding 50× at breakdown, significantly less gain is observed under alpha irradiation ($G_{alpha}$ = 1.5 and 17 for Si- and SiC-APDs, respectively), as shown in Fig. 4. We attribute the suppression of alpha-induced gain relative to optical gain to the high density of EHPs deposited along the ion track, which perturbs the local electric field and promotes carrier recombination before collection. Despite both devices falling short of their optical gain ceiling, the SiC-APD achieves approximately 11× greater alpha-induced gain than the Si-APD near their respective breakdown voltages, highlighting a significant material and/or structure-dependent difference in radiation response. The physical mechanisms responsible for this divergence are discussed in Section III.B.

### B. *Analysis of Charge Collection for 3.4 MeV Alphas*

Fig. 5 shows the simulated alpha-induced gain alongside the experimental results for both devices. The Si-APD simulation is in close agreement with experiment up to −300 V, where it predicts slightly higher gain. This is likely related to the pathlength-dependent gain mechanism mentioned in Section III.A. For the SiC-APD, the simulation captures the experimental onset of gain but underpredicts the experimental gain at −175 V. We attribute this primarily to the sensitivity of the impact ionization coefficients, especially at high electric fields. Additional uncertainty arises from the assumed device structure, doping profile, and alpha particle energy. Each of these factors affects the simulated charge deposition and electric field distribution. Despite this, the simulations closely reproduce the divergence in gain behavior between the two devices, validating their use for investigating the underlying charge collection mechanisms.

The local electric field magnitude influences carrier mobility, impact ionization rates, and recombination rates, making it a key quantity to examine during an ion strike. Fig. 6 shows the electric field profile near the breakdown voltage of the Si-APD (top) and SiC-APD (bottom) before an ion strike and 15 ps after the strike. In the Si-APD, the Bragg peak of the alpha particle lies in the high-field *n*-doped transition region, where it deposits significant charge. The sudden introduction of EHPs with densities ~2 orders of magnitude higher than the local *n*-doping screens the electric field along the ion track. The drift of electrons toward the n-contact and holes toward the *p*-contact forms a charge dipole, reducing the electric field magnitude in the center of the ion track while concentrating it at the track ends. This behavior is described by Laird *et al.* and appears here as high-field regions emerging at 15 ps, denoted a) and b) in Fig. 6. [19].

In contrast, the SiC-APD shows negligible electric field perturbation at all stages of the ion strike. The 3.4 MeV alpha particle passes completely through the thin ~2.6 µm epitaxial region, depositing most of its charge in the undepleted substrate below the avalanche region. The EHP density within the avalanche region remains insufficient to meaningfully screen the local electric field. Moreover, the heavily doped avalanche region ensures that any ion-induced EHPs represent a smaller perturbation relative to the background charge density, further limiting field distortion. As a result, the high electric field is maintained throughout the ion strike, efficiently sweeping carriers through the avalanche region and sustaining conditions favorable for impact ionization.

Fig. 7 shows the ratio of impact ionization rate to net recombination (SRH + Auger) rate for the Si-APD (top) and SiC-APD (bottom) 15 ps into an ion strike (left) and during steady-state optical generation (right). For optical generation, both devices show significant impact ionization in the depletion region. Optically-generated carriers in the depletion region are widely distributed and have a low density, minimizing recombination. The high field in the depletion region promotes significant impact ionization, resulting in the high gains observed experimentally in both devices for optical generation.

For alpha-induced charge, the Si- and SiC-APD show different responses. The Si-APD shows minimal impact ionization (ratio close to 1) in the core of the ion track, denoted c) in Fig. 7, resulting from the perturbed field suppressing impact ionization while promoting recombination. However, there is still sufficient impact ionization outside of the core. Carriers that successfully leave the core via drift/diffusion reach carrier densities low enough for impact ionization to dominate over recombination. The SiC-APD closely mirrors its optical simulation, with significant impact ionization in the depletion region despite the presence of ion-induced charge. This is a result of the heavily doped avalanche region of the SiC-APD, which reduces differences between the unperturbed space charge density and the ion-induced charge density, and thus the effects of ion-induced charge on the local field. Compared to

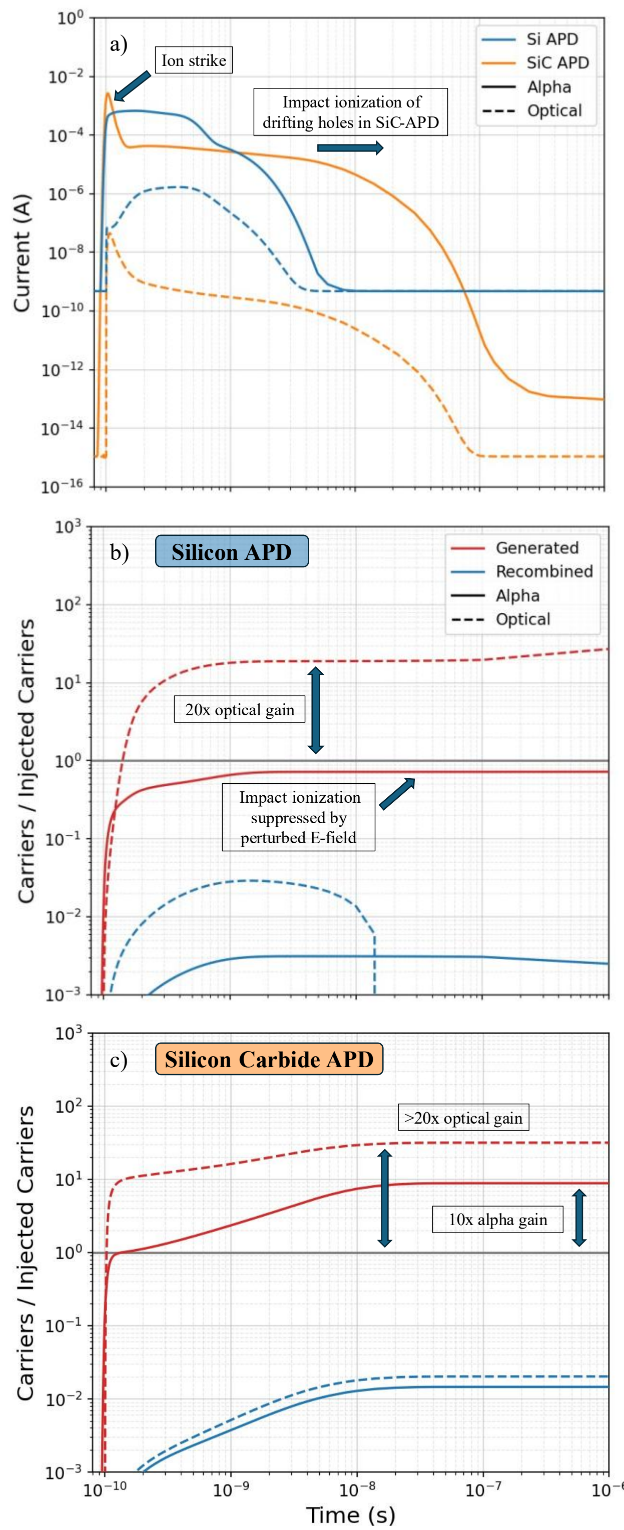


Fig. 8. Simulated a) n-contact net current and b), c) generated (red) and recombined (blue) carriers normalized to the initial number of carriers generated by an alpha particle (solid line) and an optical stimulus (dashed line) for the Si-APD and SiC-APD, respectively. The EHPs in the Si-APD are swiftly collected/recombine on the order of 10 ns. In the SiC-APD, holes in the core of the ion strike drift/diffuse into the high-field avalanche region and undergo impact ionization, leading to longer charge collection time. The perturbed electric field prevents meaningful impact ionization in the Si-APD, leading to minimal gain.

the optical simulation, more impact ionization occurs outside the core of the ion strike. Holes generated from the ion strike diffuse away from the core and drift towards the bottom contact, denoted d) in Fig. 7, resulting in a low-density carrier flux analogous to the optical simulation.

Fig. 8 shows the a) simulated current at -400 V for the Si-APD and -175 V for the SiC-APD, along with the time-integrated impact ionization-generated and recombined carrier populations, each normalized to the number of injected carriers, for the b) Si-APD and c) SiC-APD under alpha (solid line) and optical (dashed line) injection. Normalizing to the injected carrier population allows for expressing each curve as a per-carrier multiplication and recombination fraction, allowing both alpha- and optically-induced charge collection to be compared against each other at the same bias. In both devices, the current spikes immediately following the ion strike as carriers near the contacts are swept out. Beyond this initial transient, the two devices diverge. The Si-APD current decays to dark current levels within ~10 ns as carriers drift to their respective contacts or recombine before reaching them. In contrast, the SiC-APD exhibits a prolonged current transient extending to ~100 ns, associated with the delayed arrival of holes that leave the core of the ion track via drift/diffusion. As these holes enter the high-field region, they undergo impact ionization, sustaining the elevated current long after the initial strike.

Fig. 8b and 8c frame impact ionization and total recombination as carrier populations normalized to the injected carriers, providing further insight into how the two devices collect charge differently. In the Si-APD (b), optically-generated carriers undergo significant impact ionization and multiply ~20x, while the alpha-induced charge undergoes minimal impact ionization and remains below 2x gain. In both cases, recombination plays a small role in reducing the carrier population, so it cannot account for the suppressed gain alone. Instead, the perturbed electric field reduces carrier mobility inside the ion track, therefore reducing the impact ionization rate below what would be expected at a specific bias. In the SiC-APD (c), both alpha- and optically-generated carriers efficiently multiply. The electric field is minimally perturbed by the ion strike, allowing for impact ionization rates similar to optically-generated carriers. This produces the close correspondence between $G_{alpha}$ and $G_{opt}$ observed experimentally in the SiC-APD (Fig. 4), as holes entering the avalanche region have a low density reminiscent of optically-generated carrier densities.

## IV. Conclusions

Differences in charge collection between Si and SiC-APDs were evaluated during 3.4 MeV alpha irradiation. Si-APDs show minimal increase in gain as a function of applied bias, while SiC-APDs show an exponential increase in gain, with a peak 11-fold greater than that of the Si-APD. Calibrated TCAD simulations were performed to better understand the physical mechanisms causing deviations in charge collection at high biases.

In Si-APDs, the alpha particle deposits a dense EHP plasma in the high-field avalanche region, triggering significant electric field perturbation. The resulting reduction in carrier mobility leads to suppressed carrier collection and increased recombination, resulting in suppressed gain. In SiC-APDs, the thin and highly doped avalanche region prevents meaningful electric field perturbation during the ion strike. Holes generated in the core of the ion track drift/diffuse into the avalanche region and undergo hole-initiated impact ionization. The charge collection conditions (low density and spatially distributed holes) closely resemble optical excitation, explaining both the high alpha-induced gain observed in SiC-APDs and its close correspondence with the optically-induced gain curve in Fig. 4. These results highlight that structural and material differences between Si- and SiC-APDs produce fundamentally different SET responses. Future work should focus on isolating material-dependent contributions to charge collection by studying Si and SiC structures with matched epitaxial region thicknesses.

## V. Acknowledgments

Hamamatsu (Bridgewater, NJ, USA) is thanked for fabricating modified Si-APDs without epoxy and for useful technical discussions. Andrew Sternberg is acknowledged for fabrication of custom experimental setup components.

## References

[1] B. P. Abbott *et al.*, “Multi-messenger observations of a binary neutron star merger,” *Astrophys. J. Lett.*, vol. 848, no. 2, Oct. 2017, Art. no. L12.

[2] B. R. Liu, S. Xi, and X. Wang, “Neutrino emission from an off-axis jet driven by the tidal disruption event AT2019dsg,” *Phys. Rev. D*, vol. 102, no. 8, Oct. 2020, Art. no. 083028.

[3] L. Feinberg *et al.*, “Habitable worlds observatory’s concept and technology maturation: Initial feasibility and trade space exploration,” *arXiv preprint*, arXiv:2601.11803, Jan. 2026.

[4] P. Saxena *et al.*, “Innovative SiC ultraviolet instrumentation development with potential applications for the Habitable Worlds Observatory,” *J. Astron. Telesc. Instrum. Syst.*, vol. 11, no. 4, Sep. 2025, Art. no. 042225.

[5] D. Melnychuk and B. Zwieglinski, “Low-energy photon detection with PWO-II scintillators and avalanche photodiodes in applications to high-energy gamma-ray calorimetry,” *Advances in Photodiodes*, G. F. Dalla Betta, Ed. InTech, 2011, pp. 275-288.

[6] S. Goyal, A. Naik, and P. Sharma, “Characterization of silicon photomultipliers (SiPMs) for space exploration,” *Advances in Space Research*, vol. 70, no. 11, pp. 3750-3768, Dec. 2022.

[7] M. Sato *et al.*, “Reverse-type avalanche photodiode for scintillation detection and intrinsic energy resolution of BGO and CSO:Ce,” *2007 IEEE Nuclear Science Symposium Conference Record*, pp. 2023-2032, Jan. 2003.

[8] H. Niwa, J. Suda, and T. Kimoto, “Impact ionization coefficients in 4H-SiC toward ultrahigh-voltage power devices,” *IEEE Trans. Nucl. Sci.*, vol. 62, no. 10, pp. 3326-3333, Oct. 2015.

[9] H. Jeong *et al.,* “Development of wide-bandgap avalanche photodetectors for the ultraviolet spectral region,” *Advanced Photonics*, vol. 8, no. 2, Mar./Apr. 2026, art. no. 024001.

[10] Y. Tan *et al.*, “Silicon avalanche photodiode operation and lifetime analysis for small satellites,” *Opt. Express*, vol. 21, no. 14, pp. 16946-16954, Jul. 2013.

[11] Y. Zhou *et al.*, “Deep UV emitting scintillators for alpha and beta particle detection,” *Nucl. Instrum. Methods Phys. Res. A*, vol. 633, no. 1, pp. 31-35, Mar. 2011.

[12] J. Laird *et al.*, “Heavy-ion induced single-event transients in high-speed InP-InGaAs avalanche photodiodes,” *IEEE Trans. Nucl. Sci.,* vol. 50, no. 6, pp. 2225-2231, Dec. 2003.

[13] A. H. Johnston, “Radiation effects in optoelectronic devices,” *IEEE Trans. Nucl. Sci.,* vol. 60, no. 3, pp. 2054-2073, Jun. 2013.

[14] K. LaBel *et al.*, "On the suitability of fiber optic data links in the space radiation environment: A historical and scaling technology perspective," in *Proc. IEEE Aerospace Conf.*, vol. 4, pp. 421-434, Mar. 1998.

[15] J. Kommers *et al.*, "A search for non-triggered gamma-ray bursts in the BATSE data base," *Astrophys. J.*, vol. 491, no. 2, pp. 704–719, Dec. 1997.

[16] W. Zhen *et al.*, "Analysis of Single-Event Burnout in 4H-SiC Avalanche Photodiode," *IEEE Trans. Device Mater. Rel.*, vol. 25, no. 3, pp. 430–440, Sep. 2025.

[17] X. Sun *et al.*, "Space-qualified silicon avalanche-photodiode single-photon-counting modules," *J. Mod. Opt.*, vol. 51, no. 9–10, pp. 1333–1350, Jun./Jul. 2004.

[18] J. Kataoka *et al.*, "In-orbit performance of avalanche photodiode as radiation detector on board the picosatellite Cute-1.7+APD II," *J. Geophys. Res. Space Phys.*, vol. 115, no. A5, May 2010, Art. no. A05204.

[19] J. Laird *et al.*, "Quenching of impact ionization in heavy-ion induced electron-hole pair plasma tracks in wide bandwidth avalanche photodetectors," *J. Appl. Phys.*, vol. 107, no. 8, Apr. 2010, Art. no. 084501.

[20] A. Witulski *et al.*, "Single-event burnout of SiC junction barrier Schottky diode high-voltage power devices," *IEEE Trans. Nucl. Sci.*, vol. 65, no. 1, pp. 256–261, Jan. 2018.

[21] J. Lauenstein et al., "Space radiation effects on SiC power device reliability," *IEEE Int. Reliability Physics Symp. (IRPS),* Monterey, CA, Mar. 21-25, 2021, pp. 498–505.

[22] T. Makino *et al*., "Heavy-ion induced anomalous charge collection from 4H-SiC Schottky barrier diodes," *IEEE Trans. Nucl. Sci.*, vol. 60, no. 4, pp. 2647–2650, Aug. 2013.

[23] Hamamatsu Photonics, "Si APD S8664 series," KAPD1012E07 datasheet, Dec. 2020. [Online]. Available: https://www.hamamatsu.com/content/dam/hamamatsu-photonics/sites/documents/99_SALES_LIBRARY/ssd/s8664_series_kapd1012e.pdf. Accessed July 17, 2026.

[24] R. Van Overstraeten and H. De Man, "Measurement of the ionization rates in diffused silicon p-n junctions," *Solid-State Electron.*, vol. 13, no. 5, pp. 583–608, May 1970.

[25] CoolCAD Electronics, "SiC Ultraviolet Avalanche Photodiodes," CCSiCUVAPD1p1 datasheet, Feb. 2026. [Online]. Available: https://coolcadelectronics.com/wp-content/uploads/2026/02/CoolCAD_SiC_APD1p1_unpackaged_v4_5.pdf. Accessed July 17, 2026.

[26] T. Kimoto, "SiC material properties," in *Wide Bandgap Semiconductor Power Devices*, B. J. Baliga, Ed. Woodhead Publishing, 2019, pp. 21-42.

[27] Synopsys. Synopsys TCAD web page. [Online]. Available: https: //www.synopsys.com/manufacturing/tcad.html. Accessed July 17, 2026.

[28] A. G. Chynoweth, "Ionization rates for electrons and holes in silicon," *Phys. Rev.*, vol. 109, no. 5, pp. 1537–1540, Mar. 1958.

[29] J. Ziegler, M. Ziegler, and J. Biersack, "SRIM – The stopping and range of ions in matter (2010)," *Nucl. Instrum. Methods Phys. Res. B*, vol. 268, no. 11–12, pp. 1818–1823, Jun. 2010.